

## RESEARCH ARTICLE

10.1002/2015JC010711

## Key Points:

- Internal tides were observed in glider data in the vicinity of Tasmania
- Observations indicate internal tidal beam originating on the Campbell Plateau
- The tidal beam is subsequently reflected and scattered on the continental slope

## Correspondence to:

D. Boettger,  
daniel.boettger@student.adfa.edu.au

## Citation:

Boettger, D., R. Robertson, and L. Rainville (2015), Characterizing the semidiurnal internal tide off Tasmania using glider data, *J. Geophys. Res. Oceans*, 120, 3730–3746, doi:10.1002/2015JC010711.

Received 9 JAN 2015

Accepted 23 APR 2015

Accepted article online 28 APR 2015

Published online 27 MAY 2015

## Characterizing the semidiurnal internal tide off Tasmania using glider data

Daniel Boettger<sup>1</sup>, Robin Robertson<sup>1</sup>, and Luc Rainville<sup>2</sup>
<sup>1</sup>School of Physical, Environmental and Mathematical Sciences, University of New South Wales Canberra, Canberra, Australia, <sup>2</sup>Applied Physics Laboratory, University of Washington, Washington, USA

**Abstract** The spatial structure of the semidiurnal internal tide in the vicinity of Tasmania is characterized using temperature and salinity data from Seaglider and Slocum glider deployments. Wavelet analysis of isopycnal displacements measured by the gliders was used to isolate the semidiurnal internal tide, with a solid signal observed both to the east and to the south of Tasmania. The signal south of Tasmania was attributed to local forcing, while that to the east of Tasmania was found to have propagated from the south east to the north west—a result which supports previous studies indicating the presence of an internal tidal beam originating over the Macquarie Ridge, south of New Zealand. Displacement amplitudes were observed to be amplified in the vicinity of the continental slope, with the incoming tidal beam shown to be both reflected and scattered on the continental slope and shelf, and energy transferred to higher modes.

## 1. Introduction

In a stratified ocean, internal tides are produced following the interaction of the barotropic tide with topographic features such as ridges, seamounts, and the continental margins. The generation and subsequent dissipation of internal tides has been established as a key source of mixing over a wide range of spatial scales and in driving the global thermohaline circulation, providing up to half of the total energy required [Egbert and Ray, 2000, 2001; Kantha and Tierney, 1997].

Although not a region with remarkably large barotropic tidal energy, a number of features of the bathymetry of the southern Tasman Sea are ideal for internal tide generation. In particular, the Macquarie Ridge and Campbell Plateau, located south of New Zealand, have been shown to convert significant amounts of barotropic tidal energy into baroclinic tides [Egbert and Ray, 2001; Niwa and Hibiya, 2001], with results from a global baroclinic model indicating the formation of an intense tidal beam at the  $M_2$  frequency over Macquarie Ridge [Simmons *et al.*, 2004]. This beam propagates to the northwest, shoaling on the continental slope of Tasmania.

Few in situ observations with which to verify the findings from these model studies have been collected, particularly in recent years. South of New Zealand, where the internal tidal beam is predicted to originate, little description of high-frequency motions exist, aside from moorings deployed in 1979 on the eastern flank of Campbell Plateau [Heath, 1983]. On the western side of the Tasman Sea, Jones and Padman [1983] reported semidiurnal internal tides with amplitudes of up to 30 m in eastern Bass Strait; however, it is unclear how much can be inferred from this study in relation to the internal tide further offshore. Interest in internal tides propagating across the Tasman Sea has been rekindled recently, with a large field program undertaken in early 2015 (Tasmanian Tidal Dissipation Experiment (TTIDE)) [Pinkel *et al.*, 2015].

This study contributes to the observational record and provides in situ results for comparison to both model and remote sensing studies. Using observations from multiple deployments of both Seaglider and Slocum gliders along the coast of Tasmania, we assess the internal tide field, characterizing the spatial variation of the amplitude and phase, as well as estimating the temporal variance of these parameters. Details of the data used, as well as a description of the area of interest for this study are contained in sections 2.1–2.3. To deal with the spatial and temporal variability of the signal created by the movement of the glider through the region, we use wavelet analysis to quantify the amplitude of the isopycnal displacement. Our methods are described in full in section 2.4. Finally, the spatial variation of the internal tide field and its characteristics are discussed in section 3, followed by a summary in section 4.

**Table 1.** Typical Sampling Characteristics of the Seaglider and Slocum Data<sup>a</sup>

Characteristic	Seaglider	Slocum
Diving depth	1000 m	200 m
Vertical sampling rate	5–25 s	1–2 s
	0.5–2 m	0.1–0.5 m
Horizontal sampling rate		
Middle	2 h	0.25 h
	2 km	250 m
Top/bottom	0.5–4 h	0.05–0.5 h
	0.4–4 km	50–500 m
Nyquist frequency		
Middle	6 cpd	48 cpd
Top/bottom	3–24 cpd	24–240 cpd

<sup>a</sup>Horizontal sampling rates are given as typical of the middle and top/bottom of the gliders vertical profile, noting the irregularity of the sampling discussed in section 2.1.

## 2. Data and Methods

### 2.1. Glider Observations

In the last decade, autonomous underwater gliders have emerged as a valuable tool for oceanographic data collection. Since 2009, the Australian National Facility for Ocean Gliders (ANFOG) has operated a number of Seaglider and Slocum gliders in support of an overarching goal of monitoring the waters around Australia [IMOS, 2009–2014]. Although the deployments have covered a large portion of the Australian coastline, the spatial overlap between deployments has so far been limited. The south and east coasts of Tasmania, where 10 Seaglider and 16 Slocum deployments have been carried out since 2009, currently has one of the highest levels of glider data density.

Both glider types operate using similar principles [Eriksen *et al.*, 2001; Webb *et al.*, 2001]. Vertical movement is generated by changing the glider's buoyancy through the operation of an expandable and collapsible internal diaphragm, and by altering its attitude through the fore and aft movement of the battery pack. The wings then convert this vertical movement into forward movement with the result that the glider conducts a vertical sawtooth pattern through the water, surfacing regularly to update its position, send data, and receive instructions from operators ashore. In addition to a number of other parameters, both types of glider utilize a Seabird CTD to measure temperature and salinity.

The two glider models operated by ANFOG differ in their operating capabilities. Typical deployment lengths for the Slocum, as configured for these deployments, are less than 30 days, whereas the Seaglider can be deployed for many months, up to six. Of more significance for this study, the maximum deployed depth of the Seaglider was 1000 m, 5 times that of the Slocum, 200 m; consequently beyond the continental shelf, the Seaglider provides far greater vertical coverage of the ocean.

The Seaglider's deeper dive leads to a longer interval between dives and a larger separation between profiles (Table 1). While several profiles per day is well within the requirements to resolve the main tidal constituents (in terms, for example, Nyquist frequency), errors are introduced in the calculation of the isopycnal depth by the low vertical sampling rate, and in the estimation of the displacement amplitude by the low and irregular horizontal spacing between depth estimates. Rainville *et al.* [2013] demonstrated a linear relationship between the amplitude fit error and the amplitude of the background noise, with the error being largest at the bottom of the glider profile where the sampling rate is more irregular. Following Rainville *et al.* [2013], the analysis methods described in section 2.4 were modeled using a semidiurnal sinusoidal wave overlaid with random noise and varying phase, with full details of the verification process contained in the Appendix A. Data with excessive levels of background noise were discarded, and the maximum time interval over which the time series could be interpolated was limited to 6 h (2 h for Slocum data), in order to achieve an overall uncertainty in the amplitude of the wave of 0.2 m (to 95% confidence).

Of the glider deployments conducted in the area, a total of 8 Seaglider and 16 Slocum missions were used in this study. The Seaglider deployments were conducted in two main areas; hereafter denoted the Eastern and Southern regions (Figure 1). In contrast, the Slocum gliders were used specifically to conduct a repeat transect over the continental shelf within the Eastern region. Details of each deployment used in this study are listed in Table 2. Other glider deployments in the area, which contained short, incomplete records, were not used.

Each dive was binned at 1 m depth intervals, with the down and up portions of the dive binned separately to produce two vertical profiles per dive, creating a continuous time series of vertical profiles along the glider's track. Temperature and salinity observations (Figures 2a and 2b) were converted to density using TEOS-10 [McDougall and Barker, 2011], with these density fields then used to calculate the isopycnal depth at 0.01 kgm<sup>−3</sup> intervals. Finally, the displacement of the isopycnals was calculated relative to a 3 day

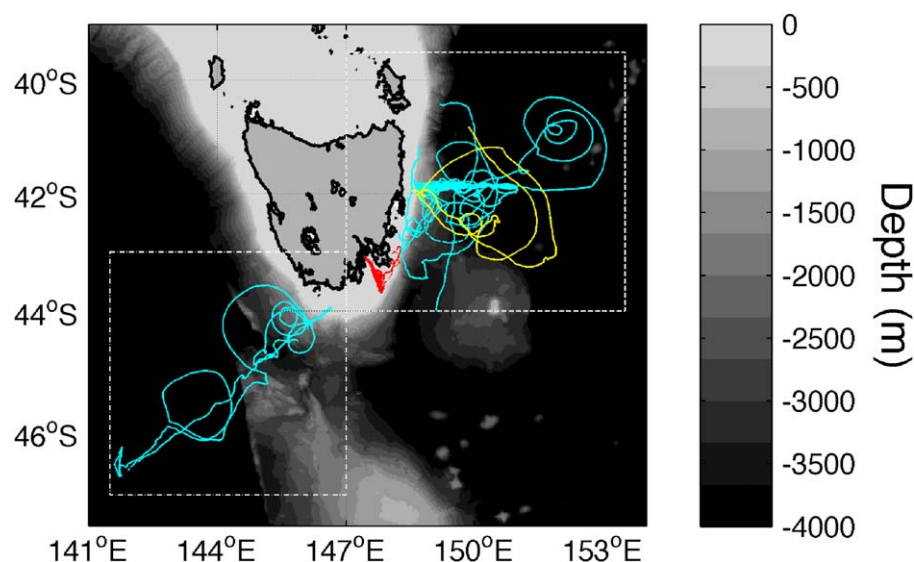


**Figure 1.** Paths of glider deployments analyzed in this study. Slocum gliders (red) are concentrated along a NW/SE transect inshore. Sea-gliders (cyan) were deployed in two main areas, here denoted East (dashed box) and South (dot-dashed box). The path of SG152, discussed later in this paper, is highlighted in yellow, with water depths (meters) shaded in gray.

running mean of the isopycnal data (Figure 2c); this window size being small enough to minimize the effect of mesoscale features while also ensuring a sufficient number of semidiurnal periods are sampled within each estimate.

A section of data from SG152 over December 2009 is shown in Figure 2. Generally, the pattern in the amplitude of the isopycnal displacement (Figure 2c) appears uniform with time; however, a period of anomalously large displacements are recorded around 6 December 2009. This coincides with the passage of the glider between a warm/cold cored eddy pair, and illustrates a change in the mean field due to the meso-scale flow. Superposed to this low-frequency signal, isopycnal displacements are dominated by rapid oscillations at approximately semidiurnal frequency,

giving an initial indication of the presence of internal tides. Further analysis, outlined below, isolates this signal from the background flow.

**Table 2.** Glider Metadata<sup>a</sup>

Glider ID	Start date	Finish date	Region	Total days
SG154	13 Feb 2009	13 Apr 2009	East	59
SG151	22 Apr 2009	22 Jun 2009	East	61
SG152	26 Nov 2009	24 Jan 2010	East	59
SG151	20 Mar 2010	03 Jun 2010	South	75
SG519	13 Aug 2010	02 Jan 2011	East	142
SG521	14 Sep 2010	24 Jan 2011	South	132
SG155	6 Apr 2011	14 Jul 2011	East	99
SG521	4 Feb 2013	8 May 2013	East	93
SL210	5 Aug 2011	24 Aug 2011	East	19
SL210	26 Sep 2011	18 Oct 2011	East	23
SL210	13 Mar 2012	4 Apr 2012	East	22
SL210	8 Jun 2012	27 Jun 2012	East	19
SL286	4 Sep 2012	21 Sep 2012	East	17
SL210	21 Sep 2012	1 Oct 2012	East	11
SL286	19 Oct 2012	4 Nov 2012	East	17
SL210	14 Nov 2012	2 Dec 2012	East	18
SL286	8 Feb 2013	26 Feb 2013	East	16
SL210	26 Feb 2013	17 Mar 2013	East	19
SL210	13 Mar 2012	4 Apr 2012	East	22
SL286	25 Mar 2013	12 Apr 2014	East	18
SL286	20 Jun 2013	9 Jul 2013	East	19
SL210	9 Jan 2014	29 Jan 2014	East	21
SL286	26 Mar 2014	16 Apr 2014	East	21
SL286	13 Jun 2014	7 Jul 2014	East	24

<sup>a</sup>Seaglider and Slocum deployments are prefixed by "SG" and "SL," respectively.

## 2.2. Bathymetry and Background Flow

The bathymetry around Tasmania is characterized by a narrow continental shelf (approximately 100 km) that descends steeply into open ocean in three directions: east, south, and west. The only major exceptions to this pattern are the East Tasman Plateau—located approximately 250 km south east of Tasmania and including the Cascade Seamount, which rises to 650 m—and the South Tasman Rise, a broad feature extending south from Tasmania with depths of less than 1000 m. On the eastern boundary of the Tasman Sea, the Macquarie Ridge extends southwest of the South Island of New Zealand, with depths generally around 1000 m. Further east, the Campbell Plateau is a broad extension of the shelf south of New Zealand. With steep, tall topography aligned near perpendicular to the barotropic flow, the Cascade Seamount, and the

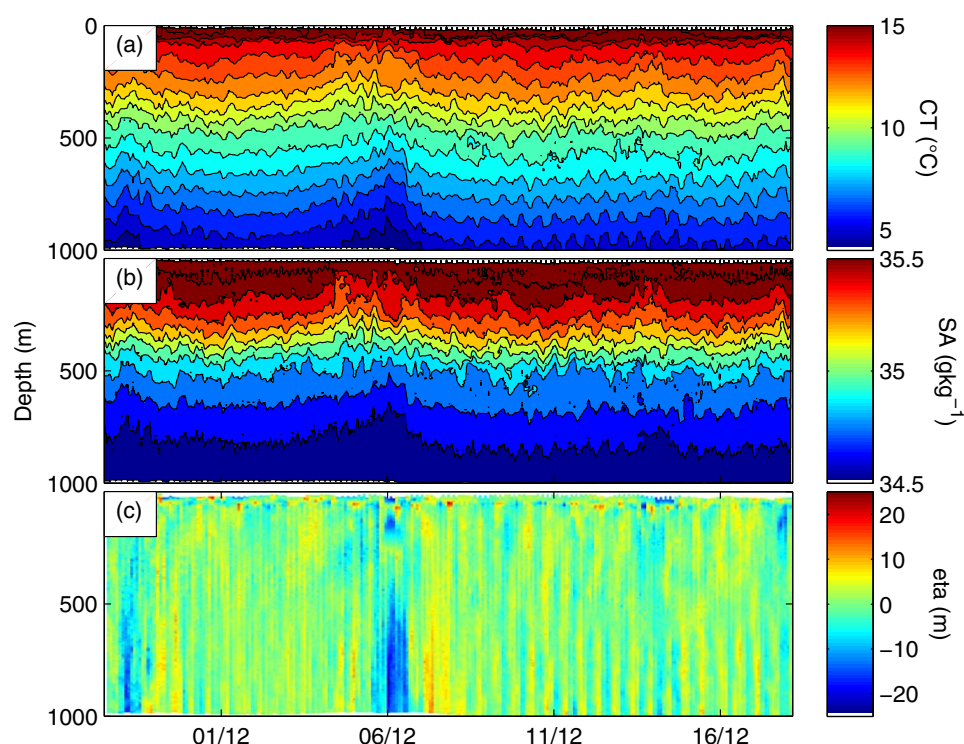


**Figure 2.** (a) Temperature, (b) salinity, and (c) isopycnal displacement for a representative period of the SG152 deployment.

Macquarie Ridge are the most likely of these features to produce a significant internal wave field [Garrett and Kunze, 2007].

Previous oceanographic studies around Tasmania have highlighted the complexity of the area; as the confluence of the Pacific Ocean to the east, the Southern Ocean to the south and the Indian Ocean to the west result in it being a dynamic location where a variety of water masses meet and interact, causing a highly seasonally dependant flow regime [Cresswell, 2000; Ridgway, 2007].

During winter, cool subantarctic waters are drawn up from the south producing a relatively weak northward current. During the summer months, a much greater degree of variability persists as the East Australian Current (EAC) extends further south, reaching its southernmost extent along the eastern Tasmanian coast, with intense warm core eddies a common flow feature [Ridgway, 2007; Ridgway and Godfrey, 1997].

### 2.3. Barotropic Tide

The largest barotropic tidal constituent in the region is the lunar semidiurnal ( $M_2$ ), with the magnitude of the major axes of the next most significant constituent,  $S_2$ , generally less than 25% of that of  $M_2$ . The major axes of the most significant diurnal constituents,  $K_1$  and  $O_1$ , have a similar magnitude to that of  $S_2$ . Noting the diurnal critical latitudes ( $\sim 27.6^\circ$  and  $30^\circ$ ) are equatorward of the study region, baroclinic diurnal tides are not expected to freely propagate and thus not have a dominant presence away from coasts. Accordingly, this paper focuses on the semidiurnal internal tides.

The barotropic  $M_2$  tidal currents are predominantly aligned perpendicular to the continental shelf (Figure 3). Major axes range from  $\sim 5 \text{ cm s}^{-1}$  in the central Tasman Sea to over  $10 \text{ cm s}^{-1}$  in the eastern Tasman Sea and over the Macquarie Ridge. With New Zealand being the location of an amphidromic point for the barotropic  $M_2$  tide, the phase increases uniformly from north to south through the Tasman Sea.

The Macquarie Ridge is also the generation site of a significant  $M_2$  internal tide beam predicted by Simmons *et al.* [2004]. After generation, this beam travels westward across the Tasman Sea to the east Tasmanian coast, and is thought to be the main contributor to the baroclinic tidal field near Tasmania.



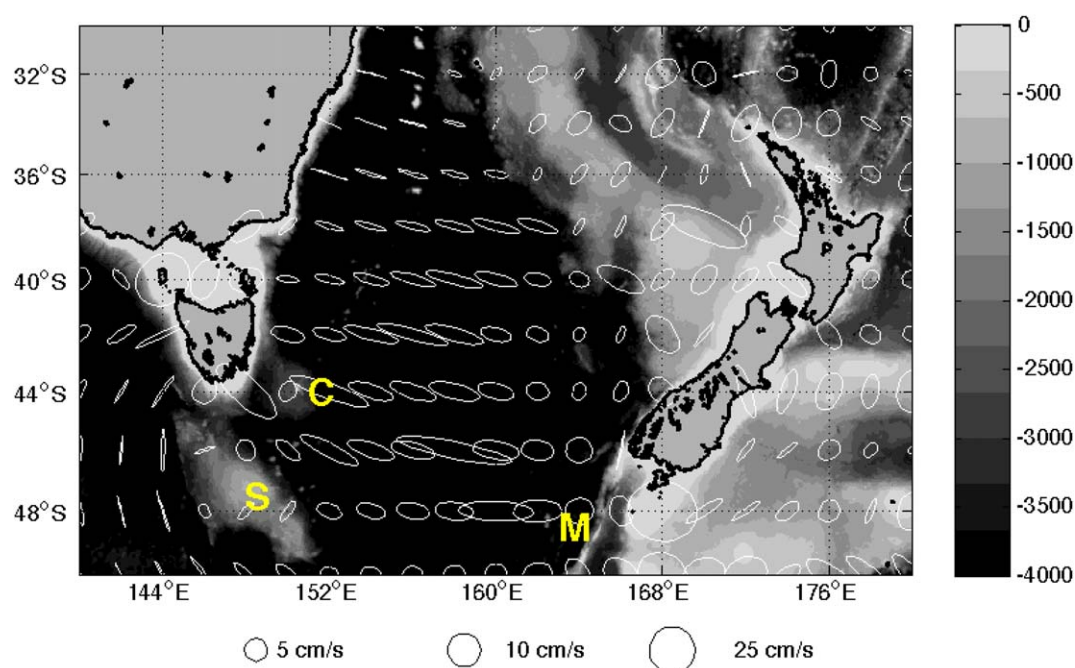


**Figure 3.**  $M_2$  barotropic tidal ellipses calculated using TPX08 data [Egbert and Erofeeva, 2002] overlaid on water depths in meters. Major bathymetric features include: the Macquarie Ridge (M), the rise located south of New Zealand; the East Tasman Plateau and the Cascade Seamount (C), located south east of Tasmania; and the South Tasman Rise (S), located south of Tasmania.

## 2.4. Estimates of the Internal Tide From Wavelets

While the mobility of the glider as an observation platform offers advantages, its movement through the water also introduces a number of complications that more traditional forms of observational data do not suffer from to the same degree. With a forward speed of around  $0.25 \text{ ms}^{-1}$ , the glider can cover distances over 20 km per day, equating to over 600 km per month. This may include periods inshore in shallow water as well as periods beyond the continental shelf. As well as this geographic variability, the glider may encounter different water masses, with a particularly pertinent note for this study being the southern incursion of the EAC and its characteristic eddy field along the east Tasmanian coast during the summer months.

Recognizing that the movement of the glider through the water, and oceanic currents themselves (in particular the strong eddies often observed to the east of Tasmania) impart a degree of Doppler smearing on the recorded time series [Rudnick and Cole, 2011], the dominant semidiurnal frequency spectral peak is expected to be smeared and shifted. Noting this, wavelet analysis was chosen as the preferred method for estimating the internal tide signal. Being well suited to detecting local changes in the intensity and frequency of signals, it has been used with glider data effectively in the past [e.g., Todd et al., 2012; Mancero-Mosquera et al., 2013]. By combining the spectral resolution of Fourier analysis with the temporal resolution of short period harmonic analysis, the method is most useful for determining the time-varying properties of the signal. Whereas Fourier analysis compares the signal of interest to a sinusoid, wavelet analysis compares the signal to a “mother wavelet.” We use the Airy wavelet [Lilly and Olhede, 2009, 2012]:

$$\psi_{\beta,\gamma}(\omega) = \int_{-\infty}^{\infty} \psi_{\beta,\gamma}(t) e^{-i\omega t} dt = U(\omega) a_{\beta,\gamma} \omega^{\beta} e^{-\omega^{\gamma}} \quad (1)$$

where  $U(\omega)$  is a unit step function and

$$a_{\beta,\gamma} \equiv 2 \left( \frac{e^{\gamma}}{\beta} \right)^{\beta/\gamma} \quad (2)$$

is a normalizing constant, while  $\beta$  and  $\gamma$  are parameters controlling the wavelet form, here set to values of 50 and 3, respectively.

The wavelet transform of a time series  $x(t)$  is described as:

$$W(s) = \frac{1}{\sqrt{s}} \int_{-\infty}^{\infty} \psi^* \left[ \frac{(t-\tau)}{s} \right] x(t) dt \quad (3)$$

where  $s$  is the *scale dilation parameter*, corresponding to the position of the center of the wavelet with respect to the time series, and  $\tau$  the *translation parameter*, which describes the width of the wavelet. The resultant amplitude and phase of the signal are then extracted from the transform by [Torrence and Compo, 1998]:

$$a = |W(s)| \quad (4)$$

$$\phi = \tan^{-1} \left[ \frac{\Im\{W(s)\}}{\Re\{W(s)\}} \right] \quad (5)$$

where  $\Im$  and  $\Re$  indicate the imaginary and real parts of  $W(s)$ , respectively.

In this study, we use the wavelet transform to characterize the temporal and spatial variability of the isopycnal displacement. The time series is initially linearly interpolated to 1 h (Seaglider) or 15 min (Slocum) intervals, chosen to be shorter than the typical profiling rate of the glider in order to preserve the variability of the signal. Edge effects are minimized by joining the ends of the time series together in order to make a periodic signal prior to conducting the transform.

The wavelet transform for the SG152 data discussed earlier is shown at Figure 4a. The most intense signal is evident around a frequency of 2 cpd. The exact frequency of the signal varies slowly with time, demonstrating the extent of the modulation of the signal by the movement of the glider and the background flow. Weaker signals at diurnal frequencies and higher frequencies are also evident. From equation (4), the calculation of the amplitude of the signal is elementary, however; determining the frequency of maximum intensity at each point in time requires further evaluation.

This was achieved using wavelet ridge analysis [Lilly and Olhede, 2010], a method for determining local maxima in the wavelet transform. Here, the range of frequencies were restricted to that which may be expected from potential Doppler smearing, so as to avoid contributions to the results from higher frequency signals. Assuming a background current speed ( $U_c$ ) of  $0.5 \text{ ms}^{-1}$ , a barotropic tidal current ( $U_T$ ) of  $2 \text{ cms}^{-1}$ , and the approximate horizontal speed of the glider ( $V_g = 0.25 \text{ ms}^{-1}$ ), the range of possible frequencies recorded by the glider are related to the  $M_2$  frequency by:

$$f_{SD} = f_{M_2} \pm \left[ \frac{(U_T + U_c)}{(U_T + V_g)} \right] \quad (6)$$

giving a frequency range of 1.63–2.45 cpd. Where more than one ridge is contained within this band, the resultant amplitude and phase of the wave is taken as the mean value. Although this band pass method does ensure the full amplitude of the signal is encompassed, it does not enable separation of the  $M_2$  and  $S_2$  constituents, and the resultant amplitude estimate contains contributions from both. Consequently, further discussion will consider  $M_2$  and  $S_2$  jointly as  $D_2$ .

The resultant amplitude of the internal  $D_2$  tidal field is illustrated in Figure 4b. The elevated displacements noted in Figure 2 are also evident here, with amplitudes of approximately double the background value. Similar periods of increased amplitudes are also seen around 27 December 2009 and 13 January 2010, particularly below 600 m; these periods again coincide with the location of the glider between a pair of eddies.

The barotropic  $D_2$  zonal currents for the two likely generation sites, the Macquarie Ridge and the Cascade Seamount, are shown at Figure 4c. While both locations exhibit a spring-neap cycle with a closely aligned phase, the relative magnitude of this cycle is much weaker at Macquarie Ridge (Table 3 and Figure 4c). Comparing the magnitudes of the barotropic currents with that of the baroclinic amplitude, it is difficult to distinguish a clear spring-neap cycle, and this is consistent with other glider deployments.

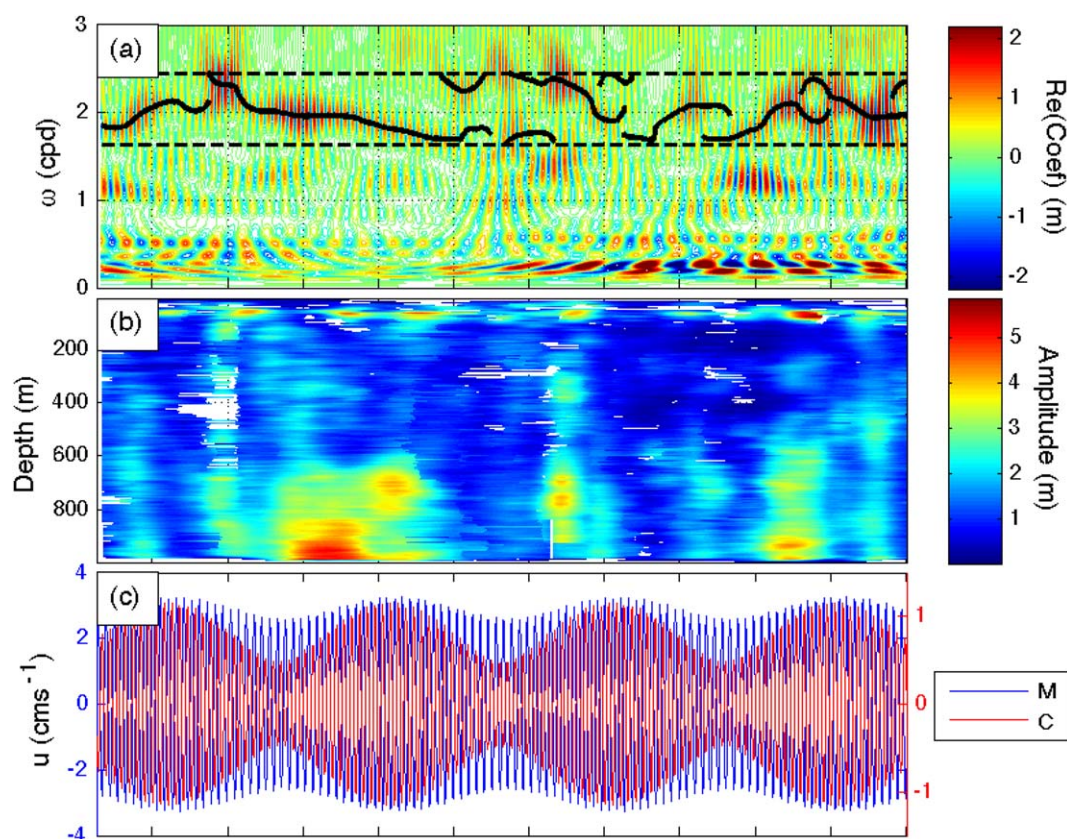


**Figure 4.** (a) The real component of the wavelet transform of SG152 during November 2009 and January 2010, at 500 m. The solid black lines are the wavelet ridges calculated within the  $D_2$  band (1.63–2.45 cpd, dashed lines) (b) The resultant amplitude of the isopycnal displacement as a function of depth. (c) The zonal  $D_2$  barotropic current for both Macquarie Ridge (M) and the Cascade Seamount (C).

### 3. Discussion

#### 3.1. Spatial Structure

In order to gauge the spatial structure of the internal wave field, amplitude estimates from the Seaglider data were binned in  $25 \times 25$  km squares, with the grid oriented parallel to the continental shelf in each region. The bin size is a compromise between the requirements to resolve the phase variation and to maintain sufficient data density within the bins—the former requiring the bin size to be less than the characteristic mode one horizontal wavelength for the region (approaching 100 km over the continental slope), and the latter satisfied by discarding any bins with less than five profiles (approximately 6%). This technique is most useful for the Eastern region, where the larger amount of data provides more spatial coverage and a greater data density (Figure 5). The most reliable estimate of the internal wave field is obtained at the middle of the glider's vertical profile, where the horizontal sampling rate is the most regular (see Appendix A for further details); for this reason the following discussion concentrates on results at 500 m.

For the Eastern region, the  $D_2$  displacement amplitude at 500 m is generally between 1 and 2 m (Figure 6). In the far southwest area of the data coverage, the amplitude is smaller—generally less than 1 m—suggesting that the propagation of the internal tide does not extend into this area. In the Southern region, the largest amplitudes are close to the continental slope before gradually becoming negligible offshore and to the south of the South Tasman Rise (Figure 7). This suggests that the generation of the internal tide field in this region is likely to occur over the local topography rather than remotely. Amplitudes inshore are larger than those estimated in the Eastern region—up to 3.5 m.

**Table 3.** Characteristics of the Spring-Neap Cycle for the Three Internal Tide Generation Sites Discussed in This Study<sup>a</sup>

Location	$M_2$ (cm s <sup>-1</sup> )	$S_2$ (cm s <sup>-1</sup> )	Ratio
South Tasman Rise (44.5°S 145°E)	1.9	0.9	2.11
Cascade Seamount (44°S 150.5°E)	2.5	1.0	2.5
Macquarie Ridge (49°S, 164.5°E)	5.0	0.7	7.14

<sup>a</sup>A smaller ratio indicates a more significant spring-neap variation.

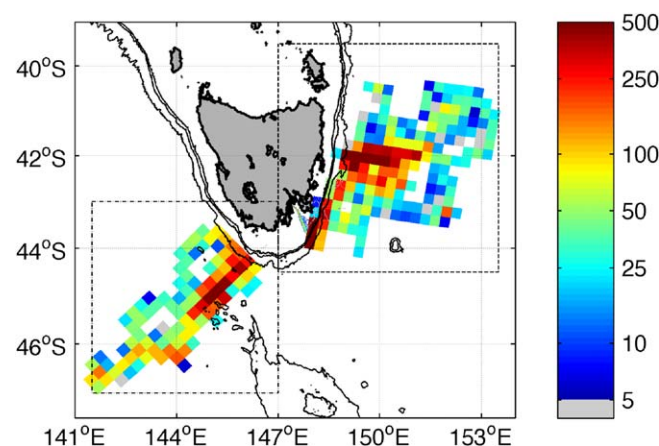


**Figure 5.** Number of glider profiles within each bin. Bins with less than five profiles are shaded gray and were discarded. The Eastern and Southern regions are denoted by the dash and dash-dot boxes, respectively. Depth contours are shown at 500, 1000, and 2000 m.

### 3.2. Spring-Neap Variation

The relative magnitudes of the  $M_2$  and  $S_2$  barotropic constituents vary across the area of interest. In the Southern region, a definite spring-neap cycle is evident in the barotropic data, likewise in the vicinity of the Cascade Seamount (Table 3). Consequently, any internal tide generated in these areas should exhibit the same cycle, with a phase lag at the location of sampling consistent with the phase speed of the wave. Conversely, the magnitude of the  $S_2$  constituent at the Macquarie Ridge is relatively insignificant when compared to the  $M_2$ , such that the spring-neap cycle at this location is minimal.

In order to quantify this effect, the magnitude of  $D_2$  isopycnal displacements during spring and neap forcing were compared. First, periods of spring and neap barotropic tides in the respective generation sites were determined using TPX08 model data [Egbert and Erofeeva, 2002], with the arrival time of the resultant internal wave at the observation site calculated assuming a mode one solution [Rainville and Pinkel, 2006]. Travel times were calculated individually for each bin, noting a difference of up to 30 h between the bins furthest offshore and those inshore. Figure 8 shows the difference between the isopycnal displacement amplitude during periods of spring and neap forcing, for bins where data from both situations were available. For the Southern region,

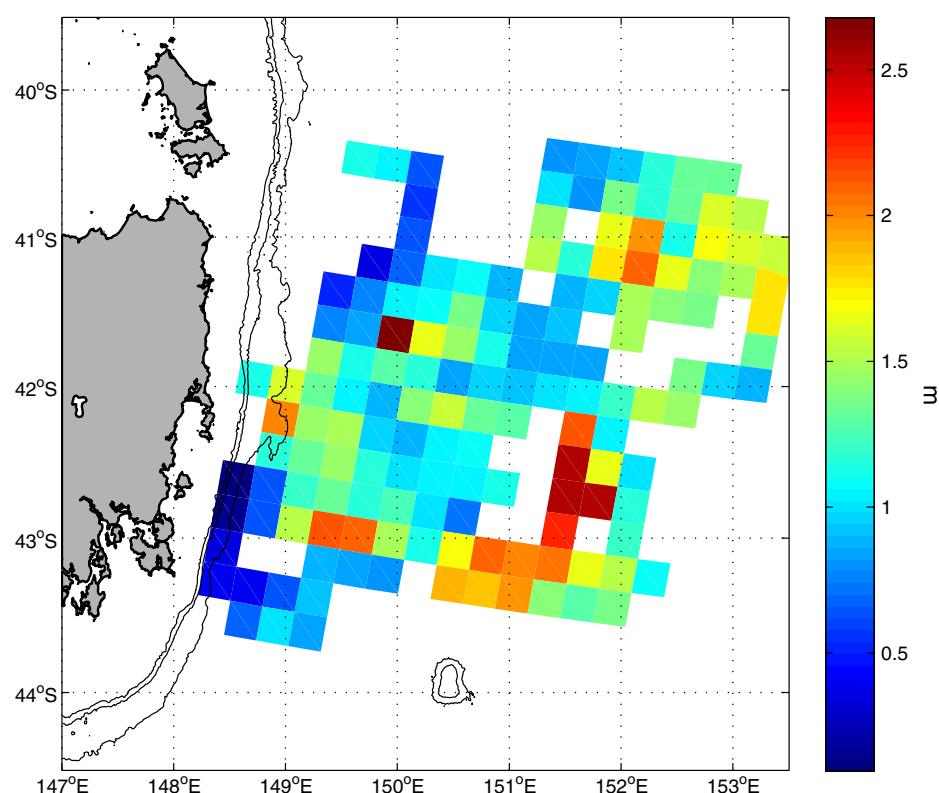


**Figure 6.** RMS  $D_2$  isopycnal displacement amplitude at 500 m depth from Seaglider deployments in the Eastern region. Depth contours are shown at 500, 1000, and 2000 m.



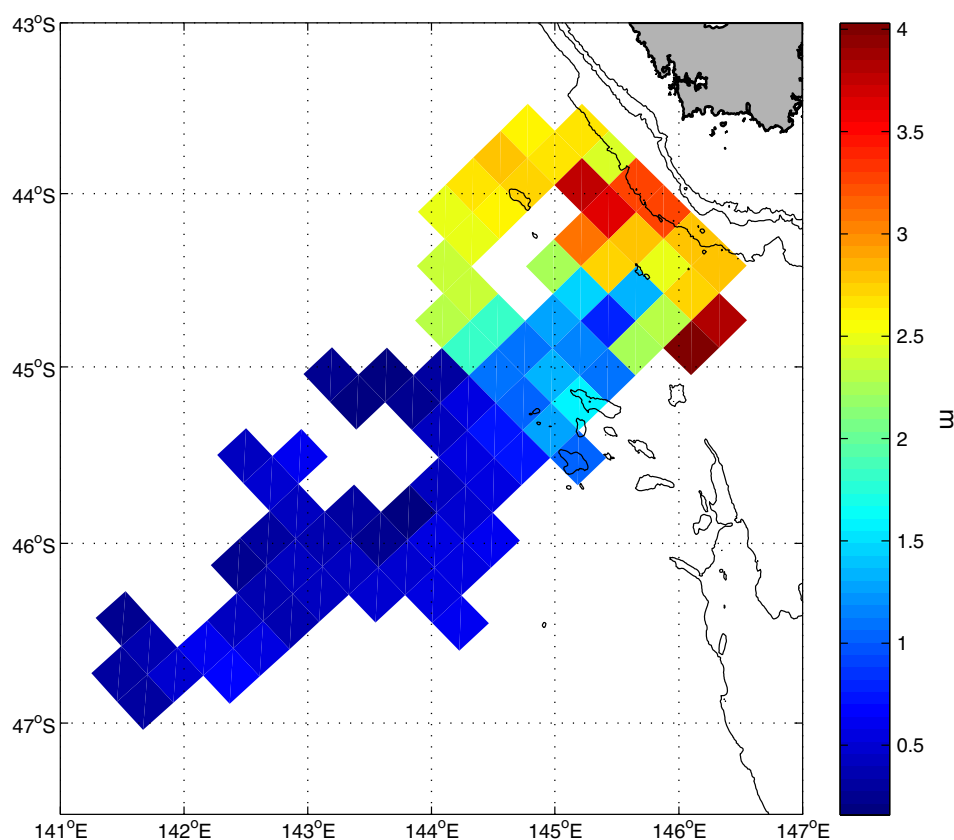


**Figure 7.** RMS  $D_2$  isopycnal displacement amplitude at 500 m depth from Seaglider deployments in the Southern region. Depth contours are shown at 500, 1000, and 2000 m.

assuming local forcing, displacement amplitudes during periods of spring tides are up to 1 m larger than during neap tides. This result not only confirms that a spring-neap cycle similar to the local barotropic forcing is evident, but also that the observed phase lag of the spring-neap cycle is consistent with local forcing. This confirms the hypothesis that the internal tide in this region is generated locally, either through interaction of the barotropic tide with the South Tasman Rise or the Tasmanian continental slope.

If the internal tide observed in the Eastern region were to originate over the Cascade Seamount, a similar spring-neap cycle would be expected off eastern Tasmania. However, no clear signal is evident, with some bins indicating larger amplitudes during periods of spring forcing and others during neap forcing. An examination of individual glider deployments (section 2.4) also indicated no clear spring-neap cycle, and the results here provide further confirmation of this observation. Consequently, if an internal tide does propagate from the Cascade Seamount toward eastern Tasmania, it is likely to be insignificant compared to other contributors to the observed internal wave field.

### 3.3. Direction of Propagation

The phase can be useful in determining the direction of propagation of the wave. Although the phase of the  $D_2$  internal tide will have contributions from both the  $M_2$  and  $S_2$  barotropic tides, the magnitude of the  $S_2$  tide is much smaller than the  $M_2$  in this region, and as such the phase of the  $D_2$  internal tide can be expressed relative to the phase of the barotropic  $M_2$  tide alone. Here we use the phase of the barotropic  $M_2$  zonal currents south east of Tasmania (at 44S 149E  $\sim$  180° GMT) as a reference phase. After binning the phase data into  $100 \times 100$  km squares, linear regression of both the zonal and meridional phase propagation was used to determine the probable direction of propagation (Figure 9). For a good fit, this method requires that only one dominant wave is being sampled, accordingly the bin size was chosen to ensure that not more than one wavelength was contained within each bin. Contamination of the signal from waves reflected or scattered on the continental slope was minimized by excluding data where the water depth is

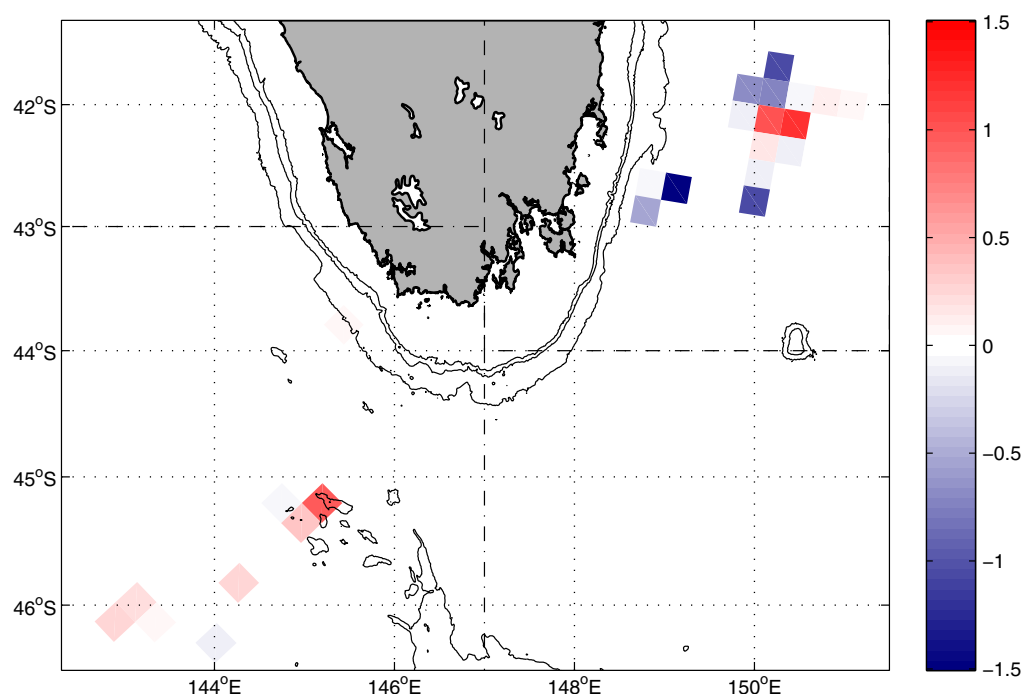


**Figure 8.** Difference between RMS  $D_2$  isopycnal displacement amplitude at 500 m for spring and neap barotropic  $D_2$  tidal forcing for the Eastern region (dashed area), assuming internal tide generation at the Cascade Seamount, and the Southern region (dash-dot area), assuming local internal tide generation. Positive (red) values indicate that the amplitudes during spring forcing are greater than for neap forcing.

less than 3000 m. Finally, any bins with a correlation between the observed phase and the regression fit less than 50% were discarded.

This method explains up to 85% of the variance of the phase of the signal when examining data from each glider individually. However, when examining all available data within each bin an average of 54% of the variance is explained. This difference in values may be explained by considering the characteristics of the mesoscale flow, particularly that of the EAC, outlined previously in section 2.2. *Rainville and Pinkel* [2006] reported that the phase of the internal wave field becomes increasingly random following

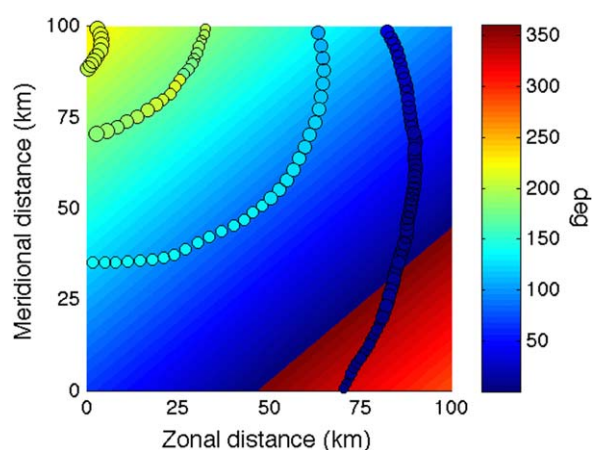


**Figure 9.** Linear regression of phase values from SG519 at 500 m for a  $100 \times 100$  km square. The original glider data are overlaid on the regression solution, with the size of the circles indicating the relative amplitude of the  $D_2$  internal tide at each position. In this example, the fit explains a total of 80% of the variance in the signal.

interaction with a barotropic mesoscale current field, and this is evident in the Eastern region when examining the standard deviation of both the amplitude and the phase (Figure 10). Here, the greatest variability coincides with the region of greatest variability in sea surface height [IMOS, 2014] and hence the area of greatest eddy activity. While this does provide challenges in isolating the mean internal tide field, the results for those bins that are less affected by the mesoscale flow all concur that the general direction of propagation of the observed  $D_2$  internal tide field is towards the WNW (Figure 11). This result correlates well with the propagation of the tidal beam predicted by *Simmons et al.* [2004] and as such, with the Cascade Seamount discounted as a primary generation site in section 3.2, the results presented here indicate

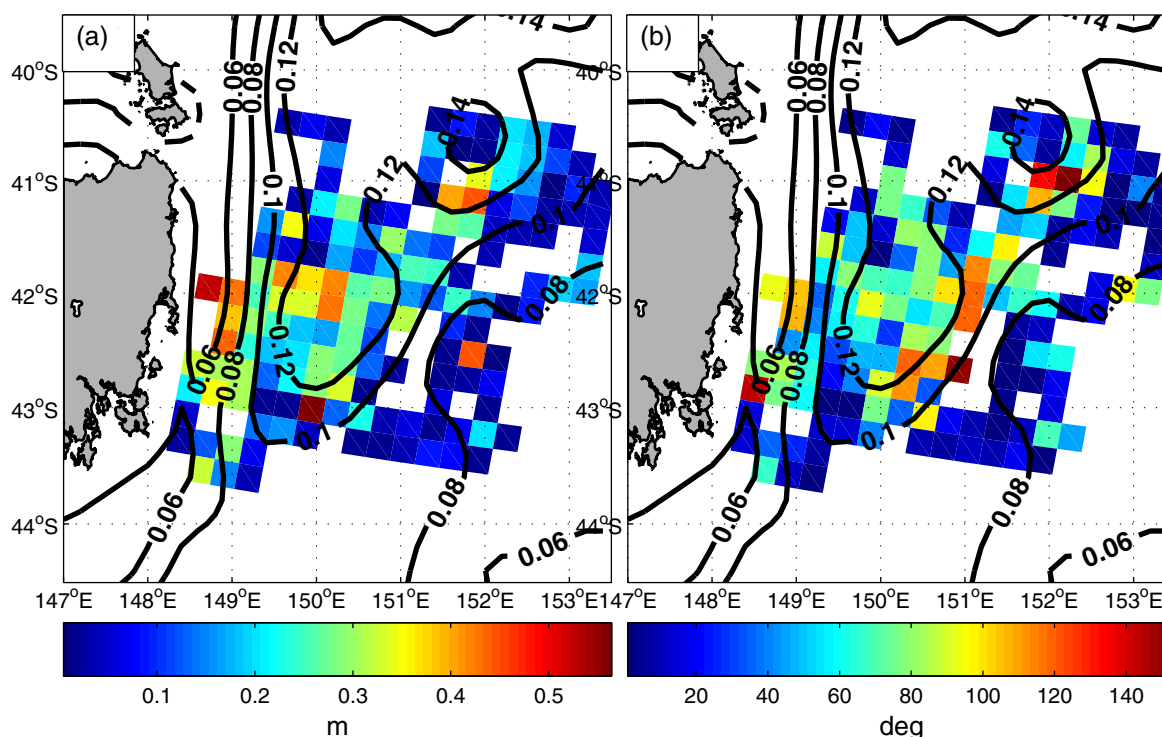


**Figure 10.** Standard deviation of the  $D_2$  displacement amplitude (a) and phase (b) at 500 m depth for the Eastern region. Contours indicate the standard deviation of the sea surface height anomaly (m) derived from satellite data over the period 2005–2013.

that the most likely source of the observed internal wave field in the Eastern region is the Macquarie Ridge.

### 3.4. Vertical Structure and Continental Shelf Interaction

Numerous studies have investigated the interaction of internal waves at the continental margins. The behavior of the incoming wave upon interaction with the margin can be predicted by the ratio between the topographical slope of the sea floor,  $s$ , and the characteristic internal wave slope,  $\alpha$ :

$$\alpha = \sqrt{\frac{\omega^2 - f^2}{N^2 - \omega^2}} \quad (7)$$

When  $s/\alpha$  is close to unity the slope is termed critical and the internal waves will propagate both up and down the slope, with a ratio less than (denoted subcritical) or greater than (denoted supercritical) unity signifying propagation of the internal wave up the slope or reflected off the slope, respectively. Climatological values of buoyancy frequency from the CSIRO Atlas of Regional Seas [Ridgway *et al.*, 2002] indicate that the topography of the eastern Tasmanian coastline is critical to supercritical. This implies that as the internal tide beam propagates from the Macquarie Ridge to the eastern Tasmania coastline, the energy will be distributed through a number of mechanisms, primarily: propagated onshore over critical topography, reflected offshore at supercritical topography, or, depending on the roughness of the slope, transferred to higher modes as the wave is scattered.

In Figure 12, the displacement amplitude is shown as a function of longitude. Although some local variation exists, the linear trend at all depths shows a constant amplitude as a function of longitude. West of  $\sim 150^\circ\text{E}$ , however, in the vicinity of the continental slope and shelf, the average amplitude of the internal wave field is larger, with a particularly significant increase in amplitude observed in the upper levels. Some degree of intensification occurs over the continental margin, likely caused by constructive interference between the incoming and reflected outgoing internal waves, or changes in stratification closer inshore.

The Slocum deployments provide a robust data set with which to investigate the propagation of the internal tide following its interaction with the continental shelf, with the 16 deployments analyzed in this study

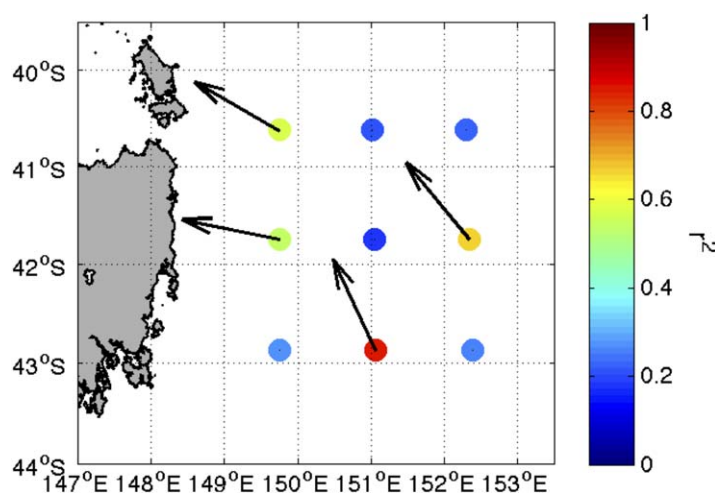


**Figure 11.** Regression of the  $D_2$  phase for all gliders in the Eastern region conducted over  $100 \times 100$  km bins. Colours represent the amount of variance explained by the fit, with unit length vectors indicating the direction of phase propagation for bins explaining more than 50% of the variance.

producing 76 repeat transects over a 3 year period. In Figure 13, isopycnal displacement amplitude data were binned over a  $1 \times 1$  km grid. A vertical transect of the data, orientated nearly perpendicular to the continental shelf, shows the amplitude of the internal tide rapidly declining towards the shore, consistent with a wave propagating onto the shelf (Figure 13a). Maximum amplitudes approach 2 m, which is approximately 70% of the internal tide amplitude at 100 m observed in the Seaglider data further offshore (not shown). Because the amplitude of the shoaling internal tide is expected to be increased, a smaller internal tide over the continental shelf suggests that only some of the incoming energy is propagating onshore. As such, while some of the energy of the incident internal tide propagates onshore, it is likely that a significant proportion is reflected by the continental slope.

With the inclination of the local  $M_2$  and  $S_2$  barotropic tide aligned perpendicular to the continental shelf, it is also possible that at least some of the internal tide field observed in the Slocum data is locally generated. If this were so, a high correlation between the baroclinic isopycnal displacement and the zonal component of the  $D_2$  barotropic tidal current just offshore would be expected. However, normalized cross correlation

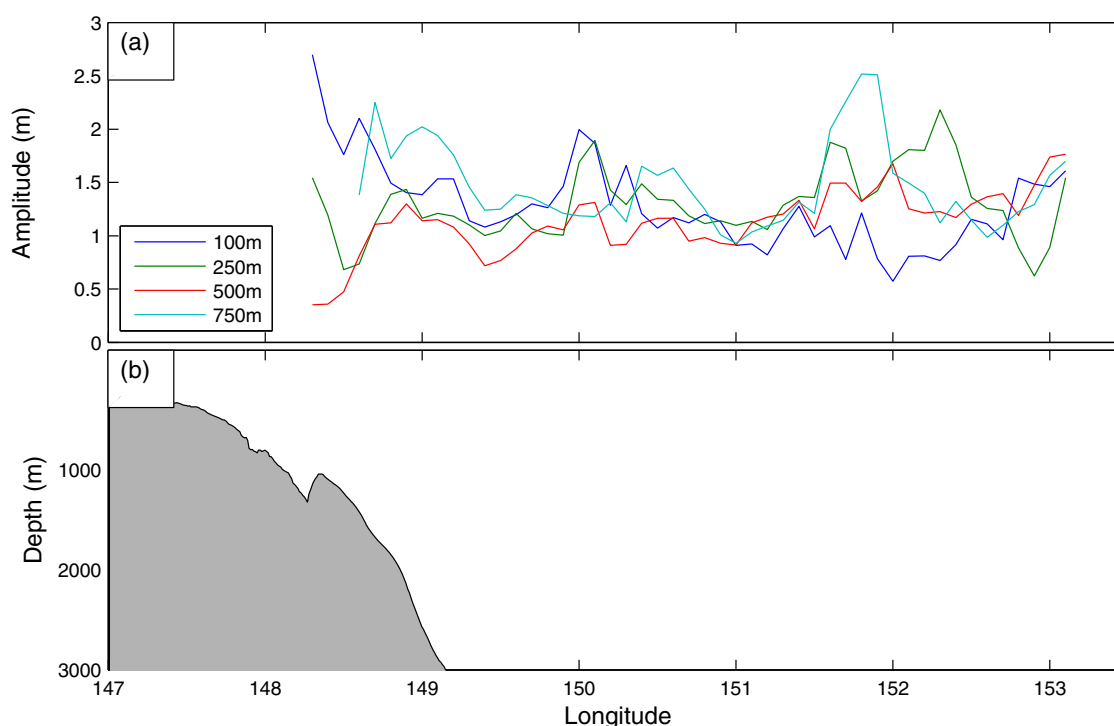


**Figure 12.** (a) Mean displacement amplitude estimates as a function of longitude for the Eastern region at various depths. (b) The typical bathymetry of the continental shelf in this region.



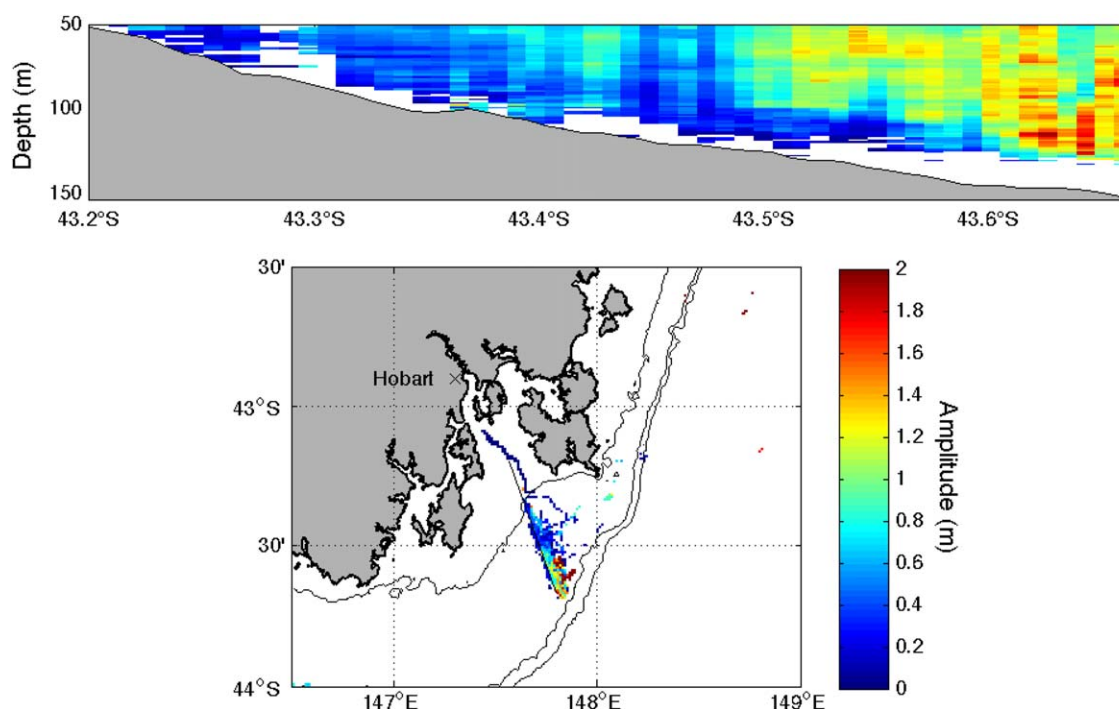


**Figure 13.** RMS  $D_2$  isopycnal displacement amplitude obtained from Slocum data from repeated transects over the continental shelf south east of Hobart. (top) The vertical structure of the  $D_2$  amplitude along a transect approximately perpendicular to the continental shelf. (bottom) The spatial variation of the amplitude at a depth of 100 m. Depth contours are shown at 100, 200, and 500 m.

values were less than 0.1 over the range of probable lags, indicating that the majority of the observed internal tide is remotely generated.

Further evidence of the reflection of the internal tide can be seen by examining the vertical distribution of the isopycnal displacement amplitude. In Figure 14, amplitude values are binned at  $1^\circ$  intervals of longitude, with the distribution of amplitude values at each depth then calculated. Around  $149^\circ\text{E}$ , in the vicinity of the continental slope, the spread of amplitude values is relatively large. Additionally, the vertical profile of the RMS amplitude is approximately constant with depth, suggesting that the wave field here is composed of a number of modes.

Further offshore, and especially within the  $152^\circ\text{E}$  bin, the vertical RMS amplitude profile begins to more closely resemble that expected from a mode one solution, with maximum displacement amplitudes likely to be below 1000 m and below the reach of the glider. This suggests that while the mode one wave dominates further offshore, the internal wave field closer inshore consists of a number of energetic modes, and lends further weight to the case of the incoming internal tide being partially reflected (and scattered) by the continental slope.

#### 4. Conclusions/Summary

Observations from Seaglider and Slocum gliders deployed along the Tasmanian coast between 2009 and 2014 were used to characterize the internal tide field in this region. Significant mesoscale activity is generated in this area by the East Australian Current. Consequently, wavelet analysis was found to be the most effective technique separating the time varying properties of the internal tide signal from these temporal disturbances to the mean flow.

Off the east coast of Tasmania, the amplitude of the  $D_2$  internal tide displacement was found to be relatively uniform. Along both the eastern and southern coasts, amplitudes in the vicinity of the continental shelf and slope were observed to be approximately twice as large as those further offshore. Of all the data analyzed, the largest amplitudes were observed over the continental slope to the southwest of Tasmania, where an

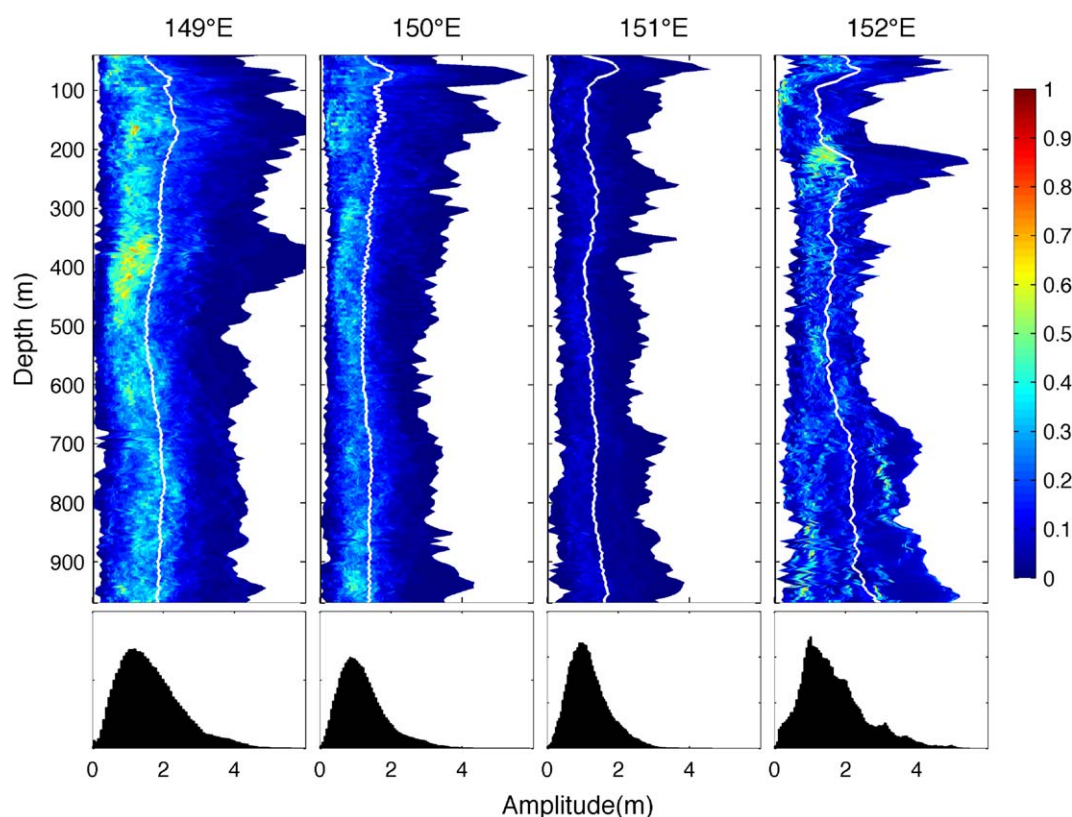


**Figure 14.** (top) Normalized distribution of the  $D_2$  displacement amplitudes for the Eastern region at each depth, binned at  $1^\circ$  longitude intervals. The RMS amplitude for each bin is plotted as the thick white line. (bottom) Distribution of the  $D_2$  displacement amplitudes over all depths for each  $1^\circ$  bin.

examination of the observed spring-neap cycle showed the internal tide to be in phase with the local barotropic tide and most likely locally generated through interaction with the South Tasman Plateau or the Tasmanian continental slope.

Off the east coast of Tasmania, the glider observations support the existence of an internal tidal beam generated south of New Zealand and propagating across the Tasman Sea. The internal wave field in this region exhibits a small spring-neap cycle, matching the variability of the barotropic tide near the Macquarie Ridge (accounting for propagation time across the Tasman Sea) better than the forcing at the local Cascade Seamount. The case for generation near the Macquarie Ridge was reinforced by using linear regression techniques to determine the direction of propagation of the  $D_2$  internal tide, which was shown to be to the northwest.

It is expected from the bathymetry and the climatological buoyancy frequency profile along the eastern coast of Tasmania that the incoming internal tidal beam will be partially reflected. While the displacement amplitude of the  $D_2$  internal tide was generally uniform offshore, a sharp increase was seen over the continental slope. Furthermore, while the typical observed vertical profile of the displacement amplitude resembled a mode one structure offshore, the profiles further inshore gradually became more complex. Slocum observations collected over the continental shelf indicate that while some of the internal tide energy propagates some distance inshore, energy is also reflected by the continental shelf. From these observations, it is likely that initially, a relatively uniform and predominantly mode one  $D_2$  internal tide propagates towards the coastline. Upon interacting with the continental slope, a large percentage of the incident energy is reflected and scattered, transferred to higher modes and subsequently interacts further with the incoming internal tide.

This study has made some preliminary findings on the characteristics and structure of the  $D_2$  internal tide in this region. More comprehensive observational programs coupled with modeling efforts, will lead to a more detailed understanding of the dynamics of internal tide in this region. The area to the east of Tasmania in

particular, warrants further investigation into the fate of the incoming tidal beam. This may provide universal insights into the interaction of internal waves with steep shelf topography.

## Appendix A: Wavelet Analysis Validation

As discussed in section 2.1, there are a number of sources of error that are unique to the glider's dive profile, the most significant of which is its slow and irregular horizontal sampling rate. The magnitude of this effect also differs with depth; in the middle of the dive, the sampling rate is relatively constant (approximately every 2 h) whereas near the bottom of the dive the glider samples twice over a short interval ( $\sim 30$  min), followed by a much longer interval of no data (up to 4 h).

Following *Rainville et al.* [2013], and with the aim of verifying the wavelet analysis methods used in this study, a series of semidiurnal sinusoidal test waves were modeled with varying phase and overlaid with random noise of varying magnitude. The phase of the wave was modeled in  $30^\circ$  increments, with the magnitude of the noise varying between 0 and 100% of the test wave amplitude. In order to represent the best and worst case scenarios, the waves were then downsampled at the rates typical of the middle and the bottom of the glider dive profile (here 450 and 900 m, respectively). As wavelet analysis requires evenly spaced data, the test waves were linearly interpolated to hourly intervals. Finally, the amplitude of the test wave was estimated using the wavelet analysis methods described in section 2.4. Figure A1, representing the worst case scenario, describes a test wave overlaid with random noise of the same magnitude and downsampled at the rate typical of the bottom of the gliders dive profile, with the resultant wavelet estimate also shown.

Figure A2 shows the magnitude of the error (to 95% confidence), averaged over all phases, as a function of noise amplitude. As would be expected, the magnitude of the error is greater using the sampling rate typical of a Seaglider at the bottom of its dive (900 m). In concurrence with *Rainville et al.* [2013], Figure A2 also shows the magnitude of the error to be a linear function of the background noise amplitude. Analysis of

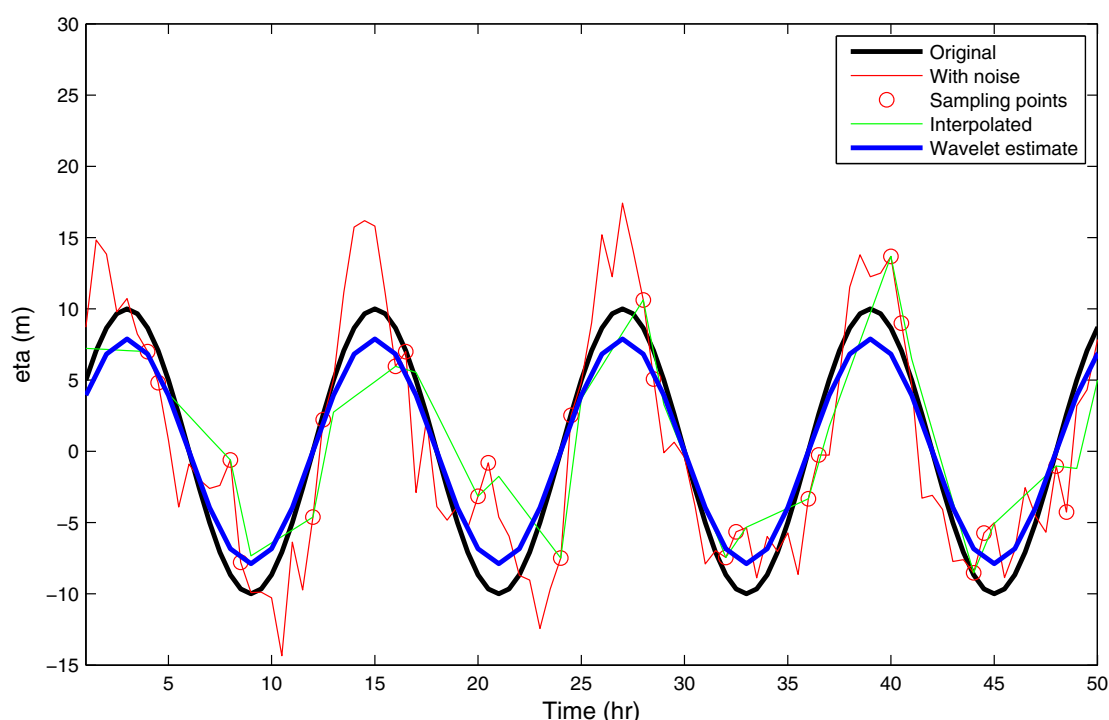


**Figure A1.** Test waves for the error analysis discussed in Appendix A. The original test wave (black) was a sinusoid with a period of 12 h, representing a semidiurnal tide. Random noise with the same amplitude as the test wave was added (red) and then the wave sampled at the irregular rate typical at the bottom of a glider profile (red circles). Finally, the wave was interpolated to 1 h intervals (green) before the wavelet analysis was performed (blue).

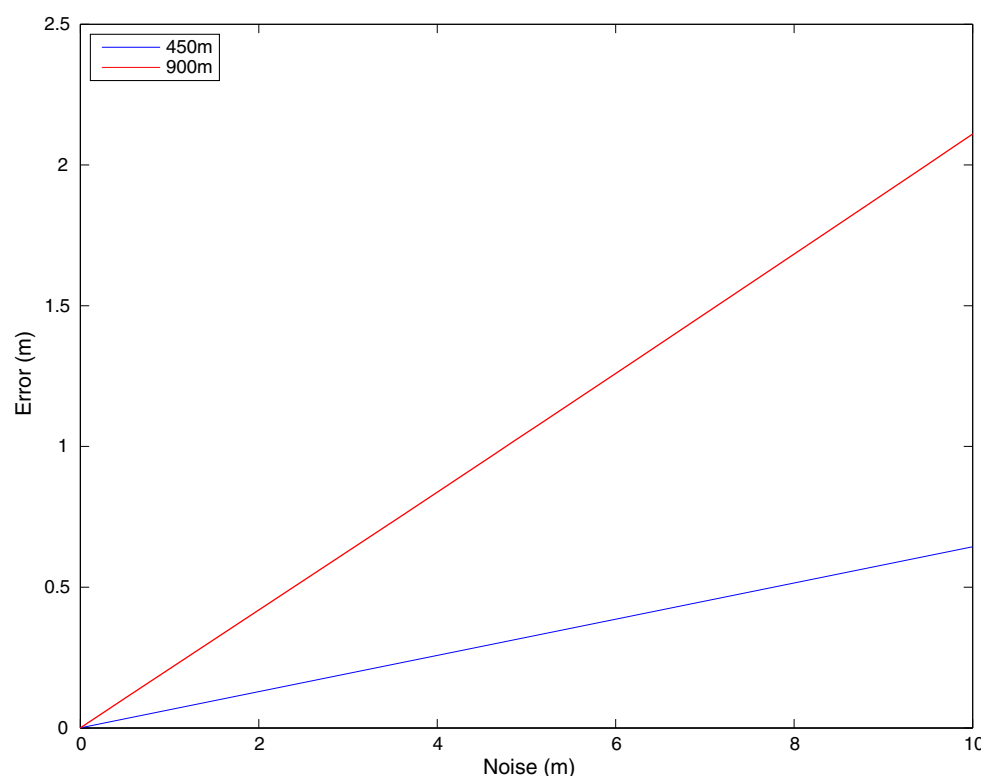


**Figure A2.** Calculation of absolute error for a semidiurnal sinusoidal wave overlaid with random noise of varying amplitude. The magnitude of the error increases linearly as a function of the amplitude of the noise.

test waves of varying initial amplitudes revealed that the magnitude of the error was the same regardless, indicating that the error is a function of the noise alone.

Following this error analysis, a number of conditions were imposed on the data. First, to address the issue of slow and irregular sampling, any data in which the amplitude of the background noise (identified through wavelet ridge analysis over the band 4–50 cpd) exceeds the amount corresponding to an uncertainty in displacement amplitude greater than 0.2 m was discarded, omitting approximately 5% of the data. Second, to avoid the introduction of excessive high-frequency noise in the time series due to interpolation, data were only interpolated over periods where the interval between data points did not exceed a certain limit (6 h for Seaglider and 2 h for Slocum data). These subsets of the time series were then discarded if their length was less than one semidiurnal period. This second condition omitted approximately 1% of data.

#### Acknowledgments

We thank two anonymous reviewers for their helpful comments. The glider data used in this paper has been collected by the Australian National Facility for Ocean Gliders, a facility of the Australian Integrated Marine Observing System. Data are available through the Australian Ocean Data Network at: <https://imos.aodn.org.au/imos123/home>.

#### References

- Cresswell, G. (2000), Currents of the continental shelf and upper slope of Tasmania, *Pap. Proc. R. Soc. Tasmania*, 133(3), 21–30.
- Egbert, G. D., and S. Y. Erofeeva (2002), Efficient inverse modeling of barotropic ocean tides, *J. Atmos. Oceanic Technol.*, 19(2), 183–204, doi:10.1175/1520-0426(2002)019.
- Egbert, G. D., and R. D. Ray (2000), Significant dissipation of tidal energy in the deep ocean inferred from satellite altimeter data, *Nature*, 405, 775–778.
- Egbert, G. D., and R. D. Ray (2001), Estimates of M2 tidal energy dissipation from TOPEX/Poseidon altimeter data, *J. Geophys. Res.*, 106(C10), 22,475–22,502, doi:10.1029/2000JC000699.
- Eriksen, C. C., T. J. Osse, R. D. Light, T. Wen, T. W. Lehman, P. L. Sabin, J. W. Ballard, and A. M. Chiodi (2001), Seaglider: A long-range autonomous underwater vehicle for oceanographic research, *IEEE J. Oceanic Eng.*, 26(4), 424–436, doi:10.1109/48.972073.
- Garrett, C., and E. Kunze (2007), Internal Tide Generation in the Deep Ocean, *Annu. Rev. Fluid Mech.* 39, 57–87, doi:10.1146/annurev.fluid.39.050905.110227.
- Heath, R. A. (1983), Tidal currents in the southwestern Pacific Basin and Campbell Plateau, southeast of New Zealand, *Deep Sea Res., Part A*, 30(4), 393–409, doi:10.1016/0198-0149(83)90074-2.
- IMOS (2009–2014), *Australian National Facility for Ocean Gliders (ANFOG): Delayed Mode Glider Deployments*. [Available at <http://thredds.aodn.org.au/thredds/catalog/IMOS/ANFOG/catalog.html>, last accessed Oct 10, 2014.]
- IMOS (2014), *Gridded Sea Level Anomaly: Delayed Mode*. [Available at <http://thredds.aodn.org.au/thredds/catalog/IMOS/OceanCurrent/GSLA/DM00/catalog.html>, last accessed Dec 12, 2014.]



- Jones, I. S. F., and L. Padman (1983), Semidiurnal internal tides in eastern Bass Strait, *Mar. Freshwater Res.*, *34*(1), 159–171, doi:10.1071/MF9830159.
- Kantha, L. H., and C. C. Tierney (1997), Global baroclinic tides, *Prog. Oceanogr.*, *40*(1–4), 163–178, doi:10.1016/S0079-6611(97)00028-1.
- Lilly, J. M., and S. C. Olhede (2009), Wavelet ridge estimation of jointly modulated multivariate oscillations, in 2009 Conference Record of the Forty-Third Asilomar Conference on Signals, Systems and Computers, pp. 452–456, IEEE, Pacific Grove, Calif., doi:10.1109/ACSSC.2009.5469858.
- Lilly, J. M., and S. C. Olhede (2010), On the analytic wavelet transform, *IEEE Trans. Inform. Theory*, *56*(8), 4135–4156, doi:10.1109/TIT.2010.2050935.
- Lilly, J. M., and S. C. Olhede (2012), Generalized morse wavelets as a superfamily of analytic wavelets, *IEEE Trans. Signal Process.*, *60*(11), 6036–6041, doi:10.1109/TSP.2012.2210890.
- Mancero-Mosquera, I., R. Gerin, E. Mauri, and P. M. Poulain (2013), Frequency content in glider data, paper presented at EGU General Assembly 2013, Vienna, Austria.
- McDougall, T. J., and P. M. Barker (2011), *Getting started with TEOS-10 and the Gibbs Seawater (GSW) Oceanographic Toolbox*, 28 pp., SCOR/IAPSO Working Group 127.
- Niwa, Y., and T. Hibiya (2001), Numerical study of the spatial distribution of the M2 internal tide in the Pacific Ocean, *J. Geophys. Res.*, *106*(C10), 22,441–22,449, doi:10.1029/2000JC000770.
- Pinkel, R., et al. (2015), Against the wall: TTIDE explores tidal mixing, scattering and reflection on the Tasmanian Continental slope, submitted to *EOS Trans. AGU*.
- Rainville, L., and R. Pinkel (2006), Propagation of low-mode internal waves through the ocean, *J. Phys. Oceanogr.*, *36*(6), 1220–1236, doi:10.1175/JPO2889.1.
- Rainville, L., C. M. Lee, D. L. Rudnick, and K.-C. Yang (2013), Propagation of internal tides generated near Luzon Strait: Observations from autonomous gliders, *J. Geophys. Res. Oceans*, *118*, 4125–4138, doi:10.1002/jgrc.20293.
- Ridgway, K. R. (2007), Seasonal circulation around Tasmania: An interface between eastern and western boundary dynamics, *J. Geophys. Res.*, *112*, C10016, doi:10.1029/2006JC003898.
- Ridgway, K. R., and J. S. Godfrey (1997), Seasonal cycle of the East Australian current, *J. Geophys. Res.*, *102*(C10), 22,921–22,936, doi:10.1029/97JC00227.
- Ridgway, K. R., J. R. Dunn, and J. L. Wilkin (2002), Ocean interpolation by four-dimensional weighted least squares: Application to the waters around Australasia, *J. Atmos. Oceanic Technol.*, *19*(9), 1357–1375, doi:10.1175/1520-0426.
- Rudnick, D. L., and S. T. Cole (2011), On sampling the ocean using underwater gliders, *J. Geophys. Res.*, *116*, C08010, doi:10.1029/2010JC006849.
- Simmons, H. L., R. W. Hallberg, and B. K. Arbic (2004), Internal wave generation in a global baroclinic tide model, *Deep Sea Res., Part II*, *51*(25–26), 3043–3068, doi:10.1016/j.dsr2.2004.09.015.
- Todd, R. E., D. L. Rudnick, M. R. Mazloff, B. D. Cornuelle, R. E. Davis, R. E. Todd, D. L. Rudnick, M. R. Mazloff, B. D. Cornuelle, and R. E. Davis (2012), Thermohaline structure in the California Current System: Observations and modeling of spice variance, *J. Geophys. Res.*, *117*, C02008, doi:10.1029/2011JC007589.
- Torrence, C., and G. P. Compo (1998), A practical guide to wavelet analysis, *Bull. Am. Meteorol. Soc.*, *79*(1), 61–78, doi:10.1175/1520-0477.
- Webb, D. C., P. J. Simonetti, C. P. Jones, D. C. Webb, P. J. Simonetti, and C. P. Jones (2001), SLOCUM: An underwater glider propelled by environmental energy, *IEEE J. Oceanic Eng.*, *26*(4), 447–452, doi:10.1109/48.972077.